

See discussions, stats, and author profiles for this publication at: <https://www.researchgate.net/publication/263952792>

Iron(III) bound by hydrosulfide anion ligands: NO-promoted stabilization of the [FeIII-SH] motif

ARTICLE in JOURNAL OF THE AMERICAN CHEMICAL SOCIETY · JUNE 2014

Impact Factor: 12.11 · DOI: 10.1021/ja503683y

CITATIONS

8

READS

37

7 AUTHORS, INCLUDING:



Chih-Chin Tsou

Yale University

11 PUBLICATIONS 191 CITATIONS

SEE PROFILE



Yun-Ming Wang

National Chiao Tung University

74 PUBLICATIONS 679 CITATIONS

SEE PROFILE



Ming-Hsi Chiang

Academia Sinica

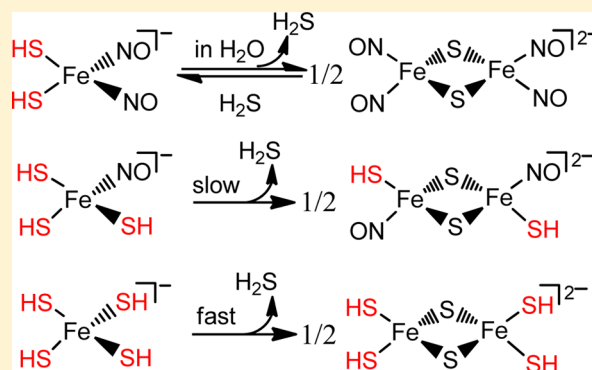
51 PUBLICATIONS 553 CITATIONS

SEE PROFILE

Iron(III) Bound by Hydrosulfide Anion Ligands: NO-Promoted Stabilization of the $[\text{Fe}^{\text{III}}-\text{SH}]$ MotifChih-Chin Tsou,^{*,†} Wei-Chun Chiu,[†] Chun-Hung Ke,[†] Jia-Chun Tsai,[‡] Yun-Ming Wang,[‡] Ming-Hsi Chiang,[§] and Wen-Feng Liaw^{*,†}[†]Department of Chemistry and Frontier Research Center on Fundamental and Applied Sciences of Matters, National Tsing Hua University, Hsinchu 30013, Taiwan[‡]Department of Biological Science and Technology, National Chiao Tung University, Hsinchu 300, Taiwan[§]Institute of Chemistry, Academia Sinica, Nankang, Taipei 115, Taiwan

S Supporting Information

ABSTRACT: Spontaneous transformation of the thermally stable $[\text{HS}]^-$ -bound $\{\text{Fe}(\text{NO})_2\}^9$ dinitrosyl iron complex (DNIC) $[(\text{HS})_2\text{Fe}(\text{NO})_2]^-$ (**1**) into $[(\text{NO})_2\text{Fe}(\mu\text{-S})]_2^{2-}$ (Roussin's red salt (RRS)) along with release of H_2S , probed by NBD-SCN (NBD = nitrobenzofurazan), was observed when DNIC **1** was dissolved in water at ambient temperature. The reversible transformation of RRS into DNIC **1** (RRS \rightarrow DNIC **1**) in the presence of H_2S was demonstrated. In contrast, the thermally unstable hydrosulfide-containing mononitrosyl iron complex (MNIC) $[(\text{HS})_3\text{Fe}^{\text{III}}(\text{NO})]^-$ (**3**) and $[\text{Fe}^{\text{III}}(\text{SH})_4]^-$ (**5**) in THF/DMF spontaneously dimerized into the first structurally characterized Fe^{III} -hydrosulfide complexes $[(\text{NO})(\text{SH})\text{Fe}(\mu\text{-S})]_2^{2-}$ (**4**) with two $\{\text{Fe}(\text{NO})\}^7$ motifs antiferromagnetically coupled and $[(\text{SH})_2\text{Fe}(\mu\text{-S})]_2^{2-}$ (**6**) resulting from two Fe^{III} ($S = 5/2$) centers antiferromagnetically coupled to yield an $S = 0$ ground state with thermal occupancy of higher spin states, respectively. That is, the greater the number of NO ligands bound to $[\text{2Fe2S}]$, the larger the antiferromagnetic coupling constant. On the basis of DFT computation and the experimental (and calculated) reduction potential ($E_{1/2}$) of complexes **1**, **3**, and **5**, the NO-coordinate ligand(s) of complexes **1** and **3** serves as the stronger electron-donating ligand, compared to thiolate, to reduce the effective nuclear charge (Z_{eff}) of the iron center and prevent DNIC **1** from dimerization in an organic solvent (MeCN).



■ INTRODUCTION

Similarly to nitric oxide (NO) and carbon monoxide (CO), hydrogen sulfide (H_2S) has recently drawn a lot of attention as an endogenously produced biological signaling molecule in the cardiovascular and nervous systems and acts as a regulator against antibiotics in the defense systems of bacteria.¹ Complex biological effects of H_2S (contraction vs relaxation of blood vessels and neurodegenerative vs neuroprotective, apoptotic vs antiapoptotic, pro-inflammatory vs anti-inflammatory, and hyperalgesic vs analgesic activities) have been reported.^{1b} These diversities in physiological functions in health and disease might be ascribed to different concentrations of H_2S and, presumably, interplay of H_2S with NO (perhaps CO).^{1f,2} H_2S –NO cross-talk is still unclear in chemical/biological systems and warrants more work in this developing area. The cooperative interaction of H_2S and NO in the regulation of angiogenesis and endothelium-dependent vasorelaxation has recently been reported.³ The reaction products between H_2S and NO display distinct biological functions compared to those regulated by H_2S and NO individually. Although H_2S cannot react with NO directly, thionitrous acid (HSNO), the smallest

S-nitrosothiol derived from the hydrosulfide anion ($[\text{SH}]^-$) and a NO^+ agent (RSNO , NO_2^-) or the hydrosulfide radical ($[\text{SH}^\bullet]$) and NO, is proposed as an effective molecule to regulate these distinct functions.^{2,4} Iron metal may participate in the interaction of H_2S and NO. In chemistry, N-bound $[\text{L}-\text{Fe}^{\text{II}}-\text{HSNO}]$ (L = porphyrin or $(\text{CN})_5$) adducts have recently been proposed as intermediates in the reaction of $\{\text{Fe}(\text{NO})\}^6$ mononitrosyl iron complexes (MNICs) and $[\text{SH}]^-$.⁵

The development of a H_2S -releasing agent, as a NO-releasing agent, for physiological use is significant. To our best knowledge, rare inorganic complexes acting as H_2S donors are known,⁶ in spite of the iron-based complex $[\text{LFe}^{\text{II}}-\text{SH}]^+$ ($\text{L} = (2\text{-CH}_2\text{Py})(\text{Me})\text{NCH}_2\text{CH}_2\text{N}(2\text{-CH}_2\text{Py})(2\text{-CH}_2\text{Py-6-N}=\text{C}(\text{tBu})\text{O}^-)$; Py = pyridine) synthesized and identified to release H_2S .⁷ The synthesis of the metal–SH motif is challenging due to its high propensity to produce multinuclear complexes, in particular, for iron.⁸ It is noticed that all of the fully characterized mononuclear iron–hydrosulfide complexes re-

Received: April 13, 2014

Published: June 10, 2014

ported are in the iron(II) state because $[\text{SH}]^-$ has a strong ability to reduce iron(III) to iron(II).^{7,8b,9} The complex $[\text{Fe}^{\text{III}}(\text{OEP})(\text{SH})]$ (OEP = octaethylporphyrin) with a ^1H NMR chemical shift of -50.0 ppm (s br, SH), quickly reduced to $[\text{Fe}^{\text{II}}(\text{OEP})]$, was observed.^{9f} Although the isolation of $[\text{Fe}^{\text{III}}(\text{T}-p\text{-OMePP})(\text{SH})]$ (T-*p*-OMePP = *meso*-tetrakis(*p*-methoxyphenyl)porphyrin) was reported,¹⁰ the identification and reproducibility of this $[\text{Fe}^{\text{III}}-\text{SH}]$ complex remain to be elucidated.^{9b,11}

The dinitrosyl iron complex (DNIC) is known to be a possible form for storage and transport of NO in biological systems.¹² NO has been demonstrated to react with $[\text{Fe}-\text{S}]$ clusters of several proteins, including mitochondrial aconitase, cytosolic aconitase, HiPIP, endonuclease III, mammalian ferrochelatase, and SoxR, to form the EPR-active DNIC with a characteristic signal at $g \approx 2.03$.¹³ The reactivity between H_2S and DNIC $[(\text{RS})_2\text{Fe}(\text{NO})_2]^-$ (and its precursors MNIC $[(\text{RS})_3\text{Fe}(\text{NO})]^-$ and $[\text{Fe}(\text{SR})_4]^-$)¹⁴ may merit further exploration to build the chemistry of NO- H_2S -Fe cross-talk. In this study, the first iron(III)-hydrosulfide complexes $[(\text{HS})_2\text{Fe}(\text{NO})_2]^-$ (**1**) and $[(\text{NO})(\text{HS})\text{Fe}(\mu\text{-S})]_2^{2-}$ (**4**) deriving from thermal conversion of $[(\text{HS})_3\text{Fe}(\text{NO})]^-$ (**3**) and $[(\text{HS})_2\text{Fe}(\mu\text{-S})]_2^{2-}$ (**6**) generated from spontaneous transformation of $[\text{Fe}(\text{SH})_4]^-$ (**5**) were isolated and characterized. Of importance, the $\{\text{Fe}(\text{NO})_2\}$ DNIC **1**, stable as a solid and in THF solution at room temperature, is demonstrated to act as a H_2S donor in aqueous solution, characterized by the H_2S probe NBD-SCN (NBD = nitrobenzofurazan). DFT computation and experimental (calculated) reduction potentials ($E_{1/2}$) of complexes **1**–**6** show that triplet NO-coordinate ligand(s) reduce the effective nuclear charge (Z_{eff}) of iron to prevent $[(\text{HS})_n\text{Fe}(\text{NO})_m]^-$ ($n = 1, 2; m = 3, 2$) motifs from autoreduction and reduce the tendency of self-rearrangement of $[(\text{HS})_n\text{Fe}(\text{NO})_m]^-$ into bis(sulfide)-bridged dimer $[(\text{L})_2\text{Fe}(\mu\text{-S})]_2^{2-}$ ($\text{L} = \text{SH}, \text{NO}$). In addition, the larger the number of NO ligands bound to the $[\text{2Fe2S}]$ core of complexes $[(\text{L})_2\text{Fe}(\mu\text{-S})]_2^{2-}$ ($\text{L} = \text{SH}, \text{NO}$), the larger the antiferromagnetic coupling constant between the two Fe cores.

RESULTS AND DISCUSSION

In the previous study, the formation pathways of the $\{\text{Fe}(\text{NO})_2\}$ DNIC $[(\text{RS})_2\text{Fe}(\text{NO})_2]^-$ from nitrosylation of the biomimetic oxidized/reduced-form rubredoxin $[\text{Fe}(\text{SR})_4]^{1-/2-}$ or the MNIC $[(\text{RS})_3\text{Fe}(\text{NO})]^-$ ($\text{R} = \text{Ph}, \text{Et}, ^t\text{Bu}$), an intermediate in the conversion of $[\text{Fe}(\text{SR})_4]^{1-/2-}$ into DNICs in the presence of NO(g), were elucidated (Scheme 1).^{14b,c,15} In contrast to treatment of the THF solution of $[(\text{PhS})_2\text{Fe}(\text{NO})_2]^-$ with $[\text{SEt}]^-$ in a 1:2 molar ratio at ambient

temperature, leading to the formation of $[(\text{EtS})_2\text{Fe}(\text{NO})_2]^-$,^{14c} the addition of 2 equiv of $[\text{SH}]^-$ to $[(\text{PhS})_2\text{Fe}(\text{NO})_2]^-$ in THF, showing the formation of the known polynuclear complexes $[\text{Fe}_4\text{S}_3(\text{NO})_7]^-$ (Roussin's black salt (RBS)) and $[(\mu\text{-S})\text{Fe}(\text{NO})_2]_2^{2-}$ (Roussin's red salt (RRS)),¹⁶ indicates that analogous $[\text{SH}]^-$ displacement does not occur. $[\text{K-18-crown-6-ether}][(\text{HS})_2\text{Fe}(\text{NO})_2]$ (**1**) (or $[\text{PPN}][(\text{HS})_2\text{Fe}(\text{NO})_2]$ (**1-PPN**)) was synthesized from the reaction of $[\text{K-18-crown-6-ether}][(\text{EtS})_2\text{Fe}(\text{NO})_2]$ (or $[\text{PPN}][(\text{EtS})_2\text{Fe}(\text{NO})_2]$)^{14b,c,17} and H_2S in THF at room temperature (Scheme 1a). Complexes **1** and **1-PPN** are thermally stable in THF and the solid state and are characterized by IR, UV-vis, EPR spectroscopy, X-ray absorption spectroscopy (XAS), and single-crystal X-ray diffraction (XRD) (Figures 1 and 2 and Supporting

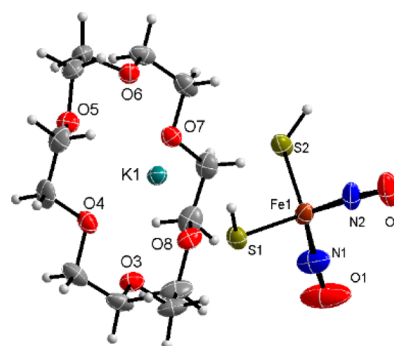
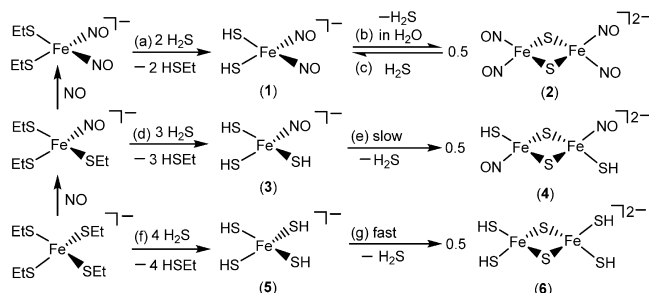


Figure 1. ORTEP drawing and labeling scheme of $[\text{K-18-crown-6-ether}][(\text{HS})_2\text{Fe}(\text{NO})_2]$ (**1**) with the thermal ellipsoid drawn at 50% probability. Selected bond lengths (Å) and angles (deg): Fe(1)–N(1), 1.676(4); N(1)–O(1), 1.177(5); Fe(1)–N(2), 1.680(4); N(2)–O(2), 1.184(5); Fe(1)–S(1), 2.2955(13); Fe(1)–S(2), 2.2987(13); S(1)–K(1), 3.4935(15); S(2)–K(1), 3.4333(15); Fe(1)–N(1)–O(1), 171.4(6); Fe(1)–N(2)–O(2), 170.5(4); N(1)–Fe(1)–N(2), 119.3(2); S(1)–Fe(1)–S(2), 109.11(5).

Information Figures S1–S4). The local geometry of complex **1** exhibits a distorted tetrahedron. The average Fe–N(O) and N–O bond lengths of DNIC **1** (Fe–N(O) = 1.678(4) Å and N–O = 1.181(5) Å) fall in the ranges of 1.661(4)–1.700(3) Å (Fe–N(O)) and 1.160(6)–1.186(3) Å (N–O) observed in the $\{\text{Fe}(\text{NO})_2\}$ DNICs (Figure 1).¹⁸ The IR ν_{NO} stretching frequencies 1735 and 1686 cm^{-1} (THF) of DNIC **1** lie between $\nu_{\text{NO}} = 1715$ and 1674 cm^{-1} for $[(\text{EtS})_2\text{Fe}(\text{NO})_2]^-$ and $\nu_{\text{NO}} = 1737$ and 1693 cm^{-1} for $[(\text{PhS})_2\text{Fe}(\text{NO})_2]^-$ (Figure S2),^{14c,19} suggesting the electron-donating ability of $[\text{SEt}]^-$, $[\text{SH}]^-$, and $[\text{SPh}]^-$ toward the $[\text{Fe}(\text{NO})_2]$ motif follows the series $[\text{SEt}]^- > [\text{SH}]^- > [\text{SPh}]^-$. Consistent with the characteristic g value of DNICs, complex **1** (or complex **1-PPN**) exhibits an isotropic EPR spectrum with a signal at $g_{\text{av}} = 2.028$ (or $g_{\text{av}} = 2.029$ and $a_{\text{N}} = 2.8$ G for **1-PPN**) at 298 K (Figure 2), indicating an $S = 1/2$ ground state. In contrast to the EPR spectrum of complex **1-PPN** showing a well-resolved five-line hyperfine splitting (Figure 2), the EPR spectrum of complex **1** displaying an isotropic signal indicates the lesser spin contribution of NO in the SOMO of complex **1**. This may be attributed to the interactions between SH/NO ligands and the [18-crown-6-ether-K] cation, which decrease the spin contribution of the NO motifs, as shown in the crystal structure. The Fe K-edge pre-edge energy of XAS is 7113.5 eV for DNIC **1**, within the range of 7113.4–7113.8 eV for $\{\text{Fe}(\text{NO})_2\}$ DNICs (Supporting Information Figure S5) (vs 7113.1–7113.3 eV for $\{\text{Fe}(\text{NO})_2\}$ DNICs).²⁰ In combination with EPR,

Scheme 1



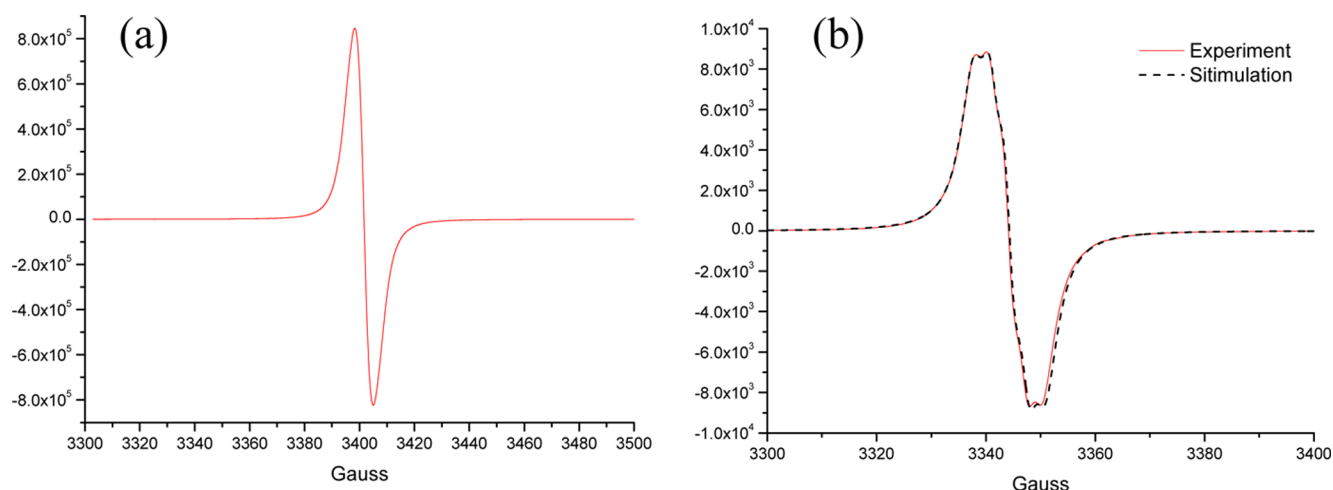
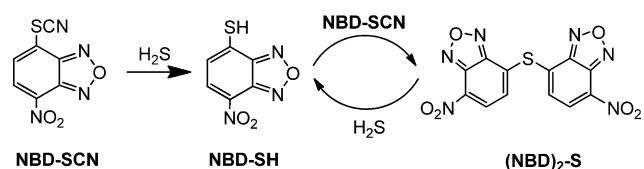


Figure 2. X-band EPR spectra of (a) DNIC **1** in THF at 298 K with $g_{av} = 2.028$ and (b) DNIC **1**-PPN in THF at 298 K with $g_{av} = 2.029$ and $a_N = 2.8$ G.

XAS, and XRD study, the dominate electronic structure of complex **1** is consistent with a high-spin Fe^{III} ($S_{\text{Fe}} = 5/2$) antiferromagnetically coupled with two NO^- anions ($S_{\text{NO}} = 1$), as observed in the previous study on DNICs.^{18a,21}

Of importance, H_2S release along with the formation of the known RRS $[\text{Fe}_2\text{S}_2(\text{NO})_4]^{2-}$ (**2**)^{16b,22} was observed when DNIC **1** was dissolved in a protic solvent (H_2O or MeOH) at room temperature (Scheme 1b). To quantitate the amount of the released H_2S derived from DNIC **1** dissolved in water, NBD-SCN, analogous to the H_2S quantification probe NBD-Cl reported recently,²³ was developed as a H_2S probe. The maximum percentage of H_2S release generated from DNIC **1** dissolved in HEPES buffer solution (pH 7.4) was determined to be 55% on the basis of a standard curve obtained from a MeOH solution (0.2 mL) of NBD-SCN and $[\text{Na}][\text{SH}]$ in 9.8 mL of HEPES buffer (40 mM, pH 7.4) (Supporting Information Figure S6). Here, we propose that the reaction of NBD-SCN and H_2S displays the same reactivity, producing NBD-SH (530 nm absorption band of NBD-SH), as the known reaction of NBD-Cl and H_2S , also yielding NBD-SH (Scheme 2).²³ Reversibly, bridged sulfide cleavage of RRS triggered by excess H_2S occurs to convert RRS back into DNIC **1**, characterized by IR and UV-vis spectroscopies (Scheme 1c).

Scheme 2. Proposed Reaction Scheme for the Reaction of NBD-SCN and H_2S



To explore the reactivity of DNIC's precursors with H_2S , MNIC $[(\text{EtS})_3\text{Fe}(\text{NO})]^-$ and $[\text{Fe}(\text{SEt})_4]^-$ were exposed to excess H_2S individually. As shown in Scheme 1d, treatment of $[(\text{EtS})_3\text{Fe}(\text{NO})]^-$ with excess H_2S in THF led to the formation of mononuclear MNIC $[(\text{HS})_3\text{Fe}(\text{NO})]^-$ (**3**), characterized by IR ($\nu_{\text{NO}} = 1728 \text{ cm}^{-1}$ (THF)) and EPR ($g_{\perp} = 3.90$ and $g_{\parallel} = 2.011$ (THF)) spectroscopies (Figure 3 and Supporting Information Figure S7a), compared to those of $[(\text{tBuS})_3\text{Fe}(\text{NO})]^-$ (IR $\nu_{\text{NO}} = 1697 \text{ cm}^{-1}$ (THF); EPR g values at 3.84 and 2.01 ($\text{CH}_2\text{Cl}_2/\text{toluene}$)) and $[(\text{PhS})_3\text{Fe}(\text{NO})]^-$ (IR $\nu_{\text{NO}} =$

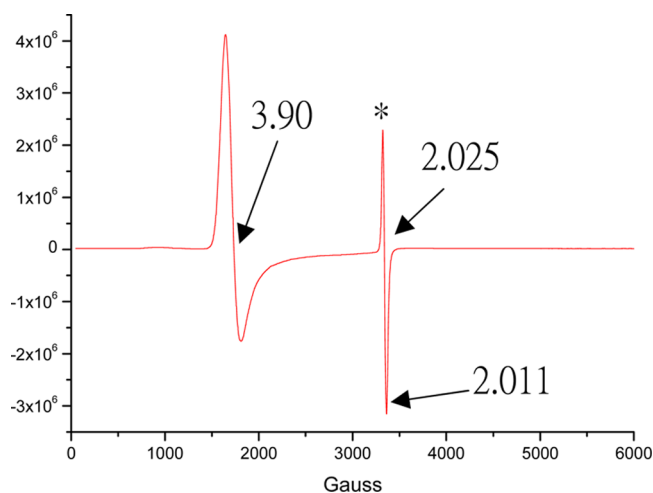


Figure 3. X-band EPR spectrum of complex **3** in THF at 4 K with $g_{\perp} = 3.90$ and $g_{\parallel} = 2.011$. The asterisk indicates the signal ($g = 2.025$) of $[(\text{HS})_2\text{Fe}(\text{NO})_2]^-$ (**1**), which derives from the reaction of a small amount of $[(\text{EtS})_2\text{Fe}(\text{NO})_2]^-$ and H_2S .

1731 cm^{-1} (THF); EPR g values at 3.76 and 2.012 ($\text{CH}_2\text{Cl}_2/\text{toluene}$)).^{14b,c} As learned from the EPR spectrum, the dominate electronic structure of MNIC **3** ($S = 3/2$, $\{\text{Fe}(\text{NO})\}^7$) is the result of strong antiferromagnetic coupling between a high-spin Fe^{III} ($S_{\text{Fe}} = 5/2$) and a NO-coordinate ligand (NO^- , $S_{\text{NO}} = 1$).²⁴ MNIC **3** in THF is thermally unstable and spontaneously dimerizes into $[(\text{NO})(\text{HS})\text{Fe}(\mu\text{-S})]_2^{2-}$ (**4**), characterized by IR ($\nu_{\text{NO}} = 1683 \text{ sh}$ and 1668 cm^{-1} (MeCN)), UV-vis, ^1H NMR spectroscopy (δ 3.49 ppm (s br, SH)), and XRD (Figure 4 and Supporting Information Figures S7b–S10), along with release of H_2S probed by NBD-SCN at room temperature overnight (Scheme 1e). Complex **4** is the first dinuclear MNIC with the local geometry of iron in a distorted tetrahedron. The mean Fe–N (1.690 Å) and N–O (1.165 Å) bond distances of complex **4** fall in the range of Fe–N(O) (1.659(6)–1.779(9) Å) and N–O (1.002(9) to 1.193(4) Å) bond lengths observed in the $\{\text{Fe}(\text{NO})\}^7$ MNICs.²⁵ The two IR ν_{NO} stretching frequencies (1683 sh and 1668 s cm^{-1} (MeCN) and 1671 s and 1651 vs cm^{-1} (KBr)) of complex **4** may arise from *trans* and *cis* isomers, albeit only the *trans* isomer is observed in the X-ray structure. ^1H

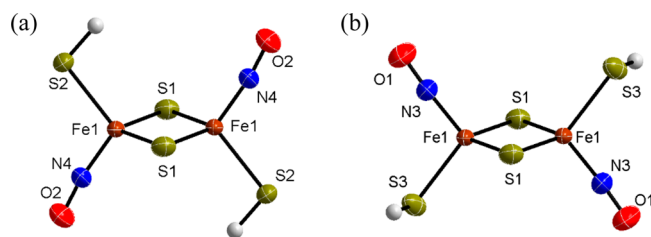


Figure 4. ORTEP drawing and labeling scheme of $[\text{PPN}]_2[(\mu\text{-S})\text{Fe}(\text{SH})(\text{NO})]_2$ (**4**) with the thermal ellipsoid drawn at 50% probability. The unit cell contains two sets of disordered $[(\mu\text{-S})\text{Fe}(\text{SH})(\text{NO})]_2^{2-}$ cores. Selected bond lengths (Å) and angles (deg) of one (51.7% (a) and 48.3% (b)) of them: (a) Fe(1)–Fe(1)#1, 2.6833(6); Fe(1)–S(1), 2.2047(7); Fe(1)–S(1)#1, 2.2117(7); Fe(1)–S(2), 2.317(2); Fe(1)–N(4), 1.685(6); N(4)–O(2), 1.169(10); Fe(1)–S(1)–Fe(1)#1, 74.83(2); S(1)–Fe(1)–S(1)#1, 105.17(2); S(2)–Fe(1)–N(4), 107.30(17); Fe(1)–N(4)–O(2), 169.0(6); (b) Fe(1)–S(3), 2.323(3); Fe(1)–N(3), 1.695(8); N(3)–O(1), 1.160(11); S(3)–Fe(1)–N(3), 104.8(2); Fe(1)–N(3)–O(1), 166.4(8). The structure of the other set is depicted in Supporting Information Figure S10.

NMR of complex **4** shows a broad peak of [SH] appearing at δ 3.49 ppm (SH, d_7 -DMF) at room temperature (Supporting Information Figure S9). Compared to the known electronic structure of RRS ($S_{\text{total}} = 0$) with two $\{\text{Fe}(\text{NO})_2\}^9$ motifs antiferromagnetically coupled,^{21b,26} complex **4** may be described as two $\{\text{Fe}(\text{NO})\}^7$ motifs antiferromagnetically coupled. The assigned $\{\text{Fe}^{\text{III}}(\text{NO})\}^7$ electronic structure of complex **4** is further supported by the broken-symmetry DFT calculation (see below). In particular, isolation of complex **4** may support the existence of the intermediate $[(\mu\text{-SR})\text{Fe}(\text{NO})(\text{SR})]_2^{2-}$ in nitrosylation of the $[2\text{Fe}_2\text{S}]$ cluster, yielding DNIC (that is, $[2\text{Fe}_2\text{S}]$ cluster $\rightarrow [(\mu\text{-SR})\text{Fe}(\text{NO})(\text{SR})]_2^{2-} \rightarrow \text{DNIC}$)²⁷ and in the repair of DNIC back into the $[2\text{Fe}_2\text{S}]$ cluster (that is, $\text{DNIC} \rightarrow \text{RRS} \rightarrow [(\mu\text{-S})\text{Fe}(\text{NO})(\text{SR})]_2^{2-} \rightarrow [2\text{Fe}_2\text{S}]$ cluster).²⁸

As shown in Scheme 1f, upon bubbling excess H_2S into a DMF solution of $[\text{Fe}(\text{SEt})_4]^-$ at 25 °C, the EPR spectrum with g values of 9.30 and 4.29 (DMF) at 4 K suggests the formation of $[\text{Fe}(\text{SH})_4]^-$ (**5**) with a high-spin Fe^{III} ($S = 5/2$) (Figure 5), compared to that of $[\text{Fe}(\text{SEt})_4]^-$ (EPR g values of 7.20 and 4.25 (DMF) at 4 K (Supporting Information Figure S11)). In

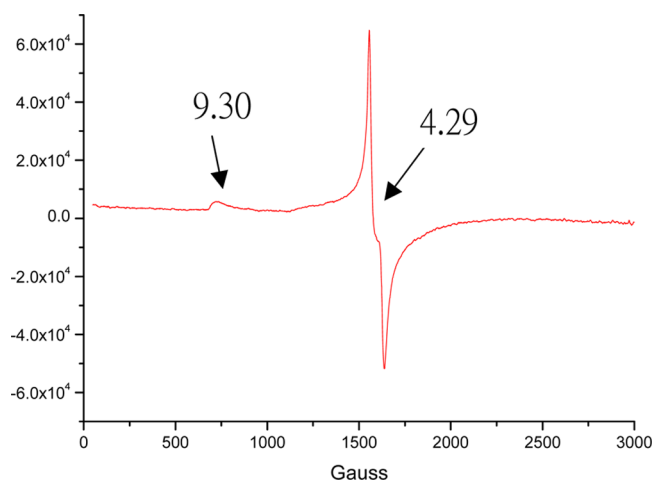


Figure 5. X-band EPR spectrum of complex **5** ($g = 9.30$ and 4.29) in DMF at 4 K.

contrast to the thermal stability of $[\text{Fe}(\text{SEt})_4]^-$,²⁹ complex **5** is thermally unstable in DMF even at -20 °C. Attempts to isolate complex **5** were unsuccessful. Quantitative transformation of complex **5** into $[(\text{HS})_2\text{Fe}(\mu\text{-S})]_2^{2-}$ (**6**), characterized by UV-vis, ^1H NMR, superconducting quantum interference device (SQUID) measurements, and XRD (Figure 6 and Supporting

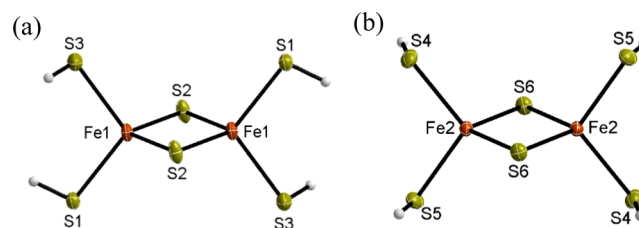


Figure 6. ORTEP drawing and labeling scheme of $[\text{PPN}]_2[(\mu\text{-S})\text{Fe}(\text{SH})_2]_2$ (**6**) with the thermal ellipsoid drawn at 50% probability. Selected bond lengths (Å) and angles (deg): (a) Fe(1)–Fe(1)#1, 2.7266(8); Fe(1)–S(1), 2.3378(9); Fe(1)–S(2), 2.2046(8); Fe(1)–S(2)#1, 2.2122(8); Fe(1)–S(3), 2.3072(9); Fe(1)–S(2)–Fe(1)#1, 76.24(3); S(2)–Fe(1)–S(2)#1, 103.76(3); S(3)–Fe(1)–S(1), 107.09(3); (b) Fe(2)–Fe(2)#2, 2.6950(7); Fe(2)–S(4), 2.3147(7); Fe(2)–S(5), 2.3165(8); Fe(2)–S(6), 2.1959(8); Fe(2)–S(6)#2, 2.2031(8); Fe(1)–S(2)–Fe(1)#1, 76.24(3); S(6)–Fe(2)–S(6)#2, 104.44(3); S(4)–Fe(2)–S(5), 110.65(3).

Information Figures S12 and S13), was demonstrated in 10 min at 0 °C (Scheme 1g). The corresponding ^1H NMR spectrum of the [SH]-coordinate ligands (δ 36.5 ppm (s br, SH)) displaying an isotropic shift, consistent with that of the oxidized $[2\text{Fe}^{\text{III}}_2\text{S}]$ clusters,^{8a} suggests that the electronic structure of the $[\text{Fe}(\mu\text{-S})_2\text{Fe}]$ core of complex **6** is best described as two Fe^{III} ($S = 5/2$) centers antiferromagnetically coupled to yield an $S = 0$ ground state with thermal occupancy of higher spin states (Figure S13a).³⁰ Magnetic susceptibility data of a microcrystalline sample of complex **6** were collected in the temperature range of 2–300 K (Figure 7). The molar magnetic

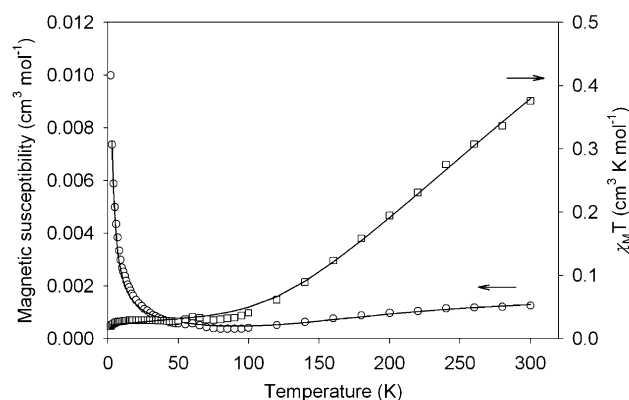


Figure 7. χ_M (open circles) and $\chi_M T$ (open squares) versus temperature for complex **6**. The solid line is the best fit of the experimental data to the theoretical model.

susceptibility increases from $1.253 \times 10^{-3} \text{ cm}^3 \text{ mol}^{-1}$ at 300 K to a value of $0.010 \text{ cm}^3 \text{ mol}^{-1}$ at 2 K. The corresponding $\chi_M T$ value decreases as a function of the temperature to $0.036 \text{ cm}^3 \text{ K mol}^{-1}$ at 95 K. The value remains practically constant until T is below 5 K and reaches $0.02 \text{ cm}^3 \text{ K mol}^{-1}$ at 2 K. The magnetic behavior of complex **6** is consistent with the observation of the oxidized $[2\text{Fe}^{\text{III}}_2\text{S}]$ clusters in the literature.^{8a} The experimental

data were fitted to an expression of the isotropic Hamiltonian, $H = JS_1S_2$, where J is the magnetic exchange integral between two Fe^{III} ($S = 5/2$) units. The stability issue of complex **6** was taken into consideration via inclusion of an Fe^{III} impurity in the theoretical expression. The least-squares fitting to the theoretical model ($\chi_{\text{obsd}} = (1 - p)\chi_{\text{FeFe}} + p\chi_{\text{imp}}$) gives $g = 2.019$, $J = 426 \text{ cm}^{-1}$, $p = 4.9 \times 10^{-3}$, and $R = 1.7 \times 10^{-3}$. The agreement factor (R) is defined as $\sum(\chi_{\text{M}}^{\text{calcd}} - \chi_{\text{M}}^{\text{obsd}})^2 / \sum(\chi_{\text{M}}^{\text{obsd}})^2$. The results suggest that a singlet-spin ground state is achieved for complex **6**.

Transformation of complex **6** into the known $[\text{Fe}_4\text{S}_4(\text{SH})_4]^{2-}$ was monitored by UV-vis and ^1H NMR (δ 47.0 ppm (s br, SH) (d_7 -DMF)) spectroscopies when complex **6** was dissolved in DMF or MeCN at ambient temperature overnight (Supporting Information Figure S13b). The shift of 309, 397, 433, 482 sh, and 585 sh nm into 368 nm confirmed the formation of $[\text{Fe}_4\text{S}_4(\text{SH})_4]^{2-}$.³¹ As shown in Table 1, the

Table 1. Selected Metric Data for $[\text{Pr}_4\text{N}]_2[(\text{NO})_2\text{Fe}(\mu\text{-S})]_2$ (2**),²² $[\text{PPN}]_2[(\text{NO})(\text{HS})\text{Fe}(\mu\text{-S})]_2$ (**4**), and $[\text{PPN}]_2[(\text{HS})_2\text{Fe}(\mu\text{-S})]_2$ (**6**)**

	2	4^c	6^c
Fe...Fe (Å)	2.704(2)	2.6833(6)	2.7266(8)
Fe-(μ -S) ^a (Å)	2.225(2)	2.2082(7)	2.2084(8)
Fe-S ^a (Å)		2.320(3)	2.3225(9)
Fe-N ^a (Å)	1.653(7)	1.690(8)	
N-O ^a (Å)	1.178(8)	1.165(11)	
(μ -S)...(μ -S) (Å)	3.535	3.508	3.474
Fe-(μ -S)-Fe (deg)	74.82(7)	74.83(2)	76.24(3)
(μ -S)-Fe-(μ -S) (deg)	105.2(1)	105.17(2)	103.76(3)
N(or S)-Fe-N(or S) (deg)	111.5(3)	106.1(2)	107.09(3)
Fe-N-O ^a (deg)	163.2(6)	167.7(8)	
dihedral angle ^b (deg)	180	180	180

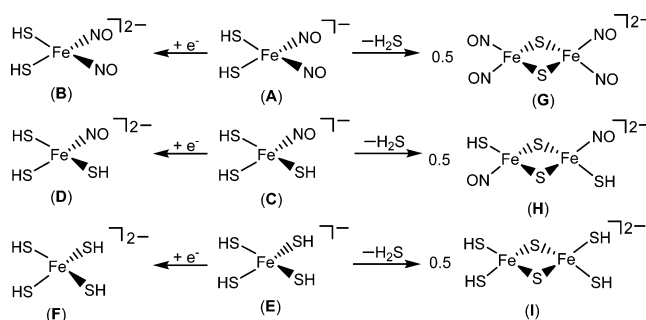
^aAverage bond distance or angle. ^bDefined by the intersection of the two $\text{Fe}_2(\mu\text{-S})$ planes. ^cSelected metric data for complexes **4** and **6** are copied from Figures 4 and 6a.

Fe...Fe bond distances of 2.704(2), 2.6833(6), and 2.7266(8) Å for complexes **2**, **4**, and **6**, respectively, suggest a weak Fe...Fe interaction. The stabilization of complexes **2** and **4** promoted by NO-coordinate ligands, compared to the instability of complex **6** slowly converting into the $[(\text{Fe}^{\text{II}})_2(\text{Fe}^{\text{III}})_2\text{S}_4(\text{SH})_4]^{2-}$ cluster, may implicate that the $[\text{Fe}(\mu\text{-S})_2\text{Fe}]$ cores of complexes **2** and **4** are tailored to preserve the $[\text{Fe}^{\text{III}}(\mu\text{-S})_2\text{Fe}^{\text{III}}]$ oxidation state, modulated by the NO-coordinate ligands. In brief, the noninnocent NO-coordinate ligand(s) bound to the $[(\text{HS})\text{Fe}^{\text{III}}(\mu\text{-S})_2\text{Fe}^{\text{III}}(\text{SH})]$ motif serves as an effective regulator to prevent the reductive elimination of the $\text{Fe}^{\text{III}}\text{-SH}$ bond of complex **4**. Measurements of the XAS S K-edge of complexes **2**, **4**, and **6** are done to rationalize the roles of NO and sulfide ligands in stabilizing complexes **2** and **4**.

It is noteworthy that the thermal stability of mononuclear complexes **1**, **3**, and **5** containing the $[\text{Fe}^{\text{III}}\text{-SH}]$ motif is in the order of $1 > 3 > 5$. That is, the $[\text{Fe}^{\text{III}}\text{-SH}]$ motif coordinated by more NO groups exhibits a reluctance to undergo self-rearrangement into the bis(sulfide)-bridged dimer $[(\text{L})_2\text{Fe}(\mu\text{-S})_2\text{Fe}(\text{L})_2]^{2-}$ ($\text{L} = \text{NO}, \text{SH}$) along with release of H_2S . The recent report shows that bridged sulfide donates more electrons to the iron center than the terminal thiolate ligand does, according to S K-edge studies of iron-sulfur clusters.³² It rationalizes that the mononuclear complexes **1**, **3**, and **5** tend to dimerize into dinuclear complexes **2**, **4**, and **6**, respectively. To

gain more information about the stability of $[\text{Fe}^{\text{III}}\text{-SH}]$ -bound complexes **1–6**, density functional theory (DFT) computation with the BP86 functional³³ and a mixed basis set of SDD ECP³⁴ on Fe, BSX_{LANL}³⁵ on S, and 6-311++G(d,p)³⁶ on all other atoms was employed on complexes **1**, **3**, and **5** and their reduced forms. This method has been determined by Hall and co-workers to exhibit accurate results for optimized geometries and NO vibrational frequencies in the $[\text{Fe}\text{-NO}]$ system.³⁷ For singlet complexes **2**, **4**, and **6**, the broken-symmetry (BS) DFT method was employed. This method provides an effective approach to estimate coupling constants in spin-coupled $[\text{Fe}\text{-NO}]$ systems and more appropriate Gibbs free energies compared to the closed-shell method.^{26,38} The comparisons of experimental parameters (complexes **1**, **2**, **4**, and **6**) and computational parameters (conformations **A**, **B**, **C**, **D**, **E**, **F**, **G**, **H**, and **I**, as shown in Chart 1) are summarized in Tables 1–3

Chart 1



and Supporting Information Tables S1–S3. The geometric parameters of conformations $[(\text{HS})_2\text{Fe}(\text{NO})_2]^{2-}$ (**A**), $[(\text{NO})_2\text{Fe}(\mu\text{-S})]_2^{2-}$ (**G**), $[(\text{NO})(\text{HS})\text{Fe}(\mu\text{-S})]_2^{2-}$ (**H**), and $[(\text{HS})_2\text{Fe}(\mu\text{-S})]_2^{2-}$ (**I**) compare well to those of complexes **1**, **2**, **4**, and **6**, respectively, except a bent dihedral angle (159.3°) in $[\text{Fe}(\mu\text{-S})_2\text{Fe}]$ of conformation **G**. The structures of computationally derived conformations $[(\text{HS})_2\text{Fe}(\text{NO})_2]^{2-}$ (**B**), $[(\text{HS})_3\text{Fe}(\text{NO})]^{2-}$ (**C**), $[\text{Fe}(\text{SH})_4]^{2-}$ (**E**), and $[\text{Fe}(\text{SH})_4]^{2-}$ (**F**) are also similar to those of $[(\text{EtS})_2\text{Fe}(\text{NO})_2]^{2-}$, $[(\text{EtS})_3\text{Fe}(\text{NO})]^{2-}$, $[\text{Fe}(\text{SET})_4]^{2-}$, and $[\text{Fe}(\text{SET})_4]^{2-}$.^{14a,c,20b,39} As shown in Tables 2, S1, and S2, the features of antiferromagnetic coupling between Fe and NO in **A**, **B**, **C**, **D**, and **H** were observed. The low spin densities of Fe and NO are ascribed to strong antiferromagnetic coupling between Fe and NO within the $[\text{Fe}(\text{NO})_x]$ motif, which leads to partial cancellation of spin

Table 2. Comparisons of Experimental and Computational Reduction Potentials

complex pair in MeCN	$E_{1/2}$ (V vs Fc^+/Fc)	ref
$[(\text{EtS})_2\text{Fe}(\text{NO})_2]^{1-/2-}$	−1.69	19
$[(\text{EtS})_3\text{Fe}(\text{NO})]^{1-/2-}$	−1.50 ^a	this work
$[\text{Fe}(\text{SET})_4]^{1-/2-}$	−1.46 ^b	29a
$[(\text{HS})_2\text{Fe}(\text{NO})_2]^{1-/2-}$	−1.55 ^c	this work
$[(\text{HS})_2\text{Fe}(\text{NO})_2]^{1-/2-}$ (A/B) (calcd)	−1.67	this work
$[(\text{HS})_3\text{Fe}(\text{NO})]^{1-/2-}$ (C/D) (calcd)	−1.62	this work
$[\text{Fe}(\text{SH})_4]^{1-/2-}$ (E/F) (calcd)	−1.17	this work
$[\text{Por}\text{-Fe}\text{-SR}]^{0/-}$ (MeOH)	−0.41 to −0.56	41

^aQuasi-reversible (Supporting Information Figure S14). ^bCalculated from $[\text{Fe}(\text{SET})_4]^{1-/2-}$ with −1.08 V (vs SCE), and the Fc^+/Fc couple occurs at +0.38 V (vs SCE) in MeCN. ^cSee Supporting Information Figure S15.

density.^{26,38b} As shown in Table 2 and Figure 8, the spin density of conformation **H** in the $M_s = 0$ broken-symmetry

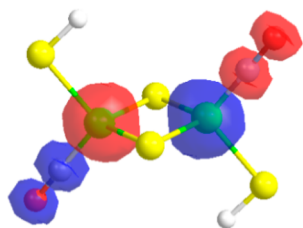


Figure 8. Broken-symmetry $M_s = 0$ spin density (isovalue 0.01) of conformation **H**.

state shows oppositely aligned spin populations on irons (2.56 for Fe_1 and -2.56 for Fe_2) and NO ligands (-0.51 for N_1O_1 and 0.51 for N_2O_2), and the plot of NO spin density displays a cylindrical symmetry. On the basis of the previous assignment of $\{\text{Fe}^{\text{III}}(\text{NO}^-)\}$ determined from the cylindrical shape of NO spin density and opposite spin densities for Fe (2.95–3.55) and NO ($-0.67 \sim -0.91$) in the $\{\text{Fe}(\text{NO})\}^7$ unit,^{24,26} the dominate electronic structure of $\{\text{Fe}(\text{NO})\}^7$ in complex **4** may be best described as a high-spin Fe^{III} ($S_{\text{Fe}} = 5/2$) antiferromagnetically coupled with a triplet NO-coordinate ligand (NO^-) ($S_{\text{NO}} = 1$).

The Heisenberg J coupling constants ($H = JS_{\text{A}}S_{\text{B}}$) (4322 cm^{-1} for **G**, 813 cm^{-1} for **H**, and 415 cm^{-1} for **I**) were calculated from the Yamaguchi equation [$J = 2(E_{\text{HS}} - E_{\text{BS}})/(\langle S^2 \rangle_{\text{HS}} - \langle S^2 \rangle_{\text{BS}})$].⁴⁰ That is, a greater number of NO ligands bound to the $[\text{2Fe2S}]$ core leads to a higher antiferromagnetic coupling constant. The larger J value is attributed to the smaller denominator in the Yamaguchi equation ($\langle S^2 \rangle_{\text{HS}} - \langle S^2 \rangle_{\text{BS}} = 2.15$ for **G**, 9.58 for **H**, and 25.79 for **I**), whereas the energy differences between high-spin and low spin-states ($E_{\text{HS}} - E_{\text{BS}}$) are quite similar.²⁶ This rationalizes why complex **2** exhibits pure singlet ground states whereas complex **6** shows a singlet ground state with thermal occupancy of higher spin states. As shown in Table 3 and Supporting Information Figures S14 and S15, the calculated reduction potentials ($E_{1/2}$) of **A/B** (-1.67 V), **C/D** (-1.62 V), and **E/F** (-1.17 V) are consistent with the trend of the experimental $E_{1/2}$ of $[(\text{EtS})_2\text{Fe}(\text{NO})_2]^{1-/2-}$ (-1.69 V), $[(\text{HS})_2\text{Fe}(\text{NO})_2]^{1-/2-}$ (-1.55 V), $[(\text{EtS})_3\text{Fe}(\text{NO})]^{1-/2-}$ (-1.50 V), and $[\text{Fe}(\text{SEt})_4]^{1-/2-}$ (-1.46 V). This result unambiguously shows that triplet NO^- serves as a stronger electron-donating ligand, compared to thiolate, in mononuclear iron complexes. Compared to the $\text{Fe}^{\text{III/II}}$ $E_{1/2} = -0.41$ to -0.56 V (vs Fc^+/ Fc) observed in octahedral the [porphyrin–Fe–SR] complex,⁴¹ the more negative $E_{1/2}$ of tetrahedral $[\text{Fe}^{\text{III}}\text{–SH}]$ complexes also explains the intrinsic difficulty of reduction of Fe^{III} in the tetrahedral system to prevent the $[\text{Fe}^{\text{III}}\text{–SH}]$ complex from autoreduction. The trend of increasing natural charge of iron from **A** (0.49) to **C** (0.72) to **E** (0.82) indicates that the triplet NO-coordinate ligand somewhat reduces the Z_{eff} of iron (Supporting Information Tables S1–S3). This result is supported by the previous S K-edge study on $[(\text{PhS})_2\text{Fe}(\text{NO})_2]^-$, $[(\text{PhS})_3\text{Fe}(\text{NO})]^-$, and $[\text{Fe}(\text{SPh})_4]^-$ showing the oxidation state of Fe, estimated from S K-edge data, is 2.75 for $[(\text{PhS})_3\text{Fe}(\text{NO})]^-$ and 2.59 for $[(\text{PhS})_2\text{Fe}(\text{NO})_2]^-$.^{21a} Presumably, the Z_{eff} of iron in **A**, **C**, and **E** reflects the stability of complexes **1**, **3**, and **5**. Specifically, the higher Z_{eff} of iron shows a preference to rearrange into a dimer with strong electron-donating bridged sulfide ligands. Moreover, the reaction free energy values (-0.6 kcal/mol for **A** to **G**, -6.8 kcal/mol for **C**

Table 3. Selected Computational Geometry Parameters, Natural Charge, Mulliken Spin Density, NO Vibrational Frequencies, Heisenberg J Coupling Constant, and Reaction Free Energy for $[(\text{NO})_2\text{Fe}(\mu\text{-S})_2\text{Fe}(\text{NO})_2]^{2-}$ (**G**), $[(\text{NO})(\text{HS})\text{Fe}(\mu\text{-S})_2\text{Fe}(\text{SH})(\text{NO})]^{2-}$ (**H**), and $[(\text{HS})_2\text{Fe}(\mu\text{-S})_2\text{Fe}(\text{SH})]^{2-}$ (**I**)

	G	H	I
Fe...Fe (Å)	2.68	2.724	2.721
Fe–($\mu\text{-S}$) ^a (Å)	2.245	2.238	2.231
Fe–S ^a (Å)		2.347	2.349
Fe–N ^a (Å)	1.647	1.685	
N–O ^a (Å)	1.203	1.194	
($\mu\text{-S}$)...($\mu\text{-S}$) (Å)	3.569	3.553	3.535
Fe–($\mu\text{-S}$)–Fe ^a (deg)	73.3	75	75.2
($\mu\text{-S}$)–Fe–($\mu\text{-S}$) ^a (deg)	105.3	105	104.8
N(or S)–Fe–N(or S) ^a (deg)	112.4	103.9	105.3
Fe–N–O ^a (deg)	163.7	169.9	
dihedral angle ^b (deg)	159.3	180	180
Mulliken spin density of Fe_1	2.47 ^d	2.56	3.37
Mulliken spin density of $\text{N}_1\text{–O}_1$	$-0.36, -0.32^e$	$-0.29, -0.22$	
Mulliken spin density of $\text{N}_3\text{–O}_3$	$-0.36, -0.33^e$		
Mulliken spin density of Fe_2	-2.47^e	-2.56	-3.37
Mulliken spin density of $\text{N}_2\text{–O}_2$	$0.36, 0.32^e$	$0.29, 0.22$	
Mulliken spin density of $\text{N}_4\text{–O}_4$	$0.36, 0.33^e$		
IR ν_{NO} (cm^{-1}) (MeCN)	1695, 1655, 1561, 1542	1630	
$\langle S^2 \rangle_{\text{HS}}$	5.02 ^e	12.42	30.02
$\langle S^2 \rangle_{\text{BS}}$	2.87 ^e	2.84	4.23
Heisenberg J coupling constant ^c (cm^{-1})	4322 ^e	813	415
reaction free energy ΔG^d (kcal/mol)	-0.6	-6.8	-15.1

^aAverage bond distance, angle, charge, or spin density. ^bDefined by the intersection of the two $\text{Fe}_2(\mu\text{-S})$ planes. ^c J value ($H = JS_{\text{A}}S_{\text{B}}$) calculated from the Yamaguchi equation: $J = 2(E_{\text{HS}} - E_{\text{BS}})/(\langle S^2 \rangle_{\text{HS}} - \langle S^2 \rangle_{\text{BS}})$.⁴⁰ $S_{\text{A}} = S_{\text{B}} = 1/2$ for **G**. $S_{\text{A}} = S_{\text{B}} = 3/2$ for **H**. $S_{\text{A}} = S_{\text{B}} = 5/2$ for **I**. ^dReaction free energy derived from the dimerization reaction $2[(\text{L})_2\text{Fe}(\text{SH})_2]^- \rightarrow 2\text{H}_2\text{S} + [(\text{L})_2\text{Fe}(\mu\text{-S})_2\text{Fe}(\text{L})_2]^{2-}$ ($\text{L} = \text{NO}, \text{SH}$). ^eDue to the very strong antiferromagnetic coupling in conformation **G**, the BP86 wave function (pure functional) collapses to a spin-restricted solution, similarly to the OLYP wave function (pure functional) in the previous study.²⁶ The values of the spin density and coupling constant are adopted from the broken-symmetry calculation with the hybrid functional B3LYP/6-311G(d,p)/COSMO electronic structure at the OLYP/TZP/COSMO geometry.²⁶ Pure functionals have been shown to result in a lesser degree of spin polarization than hybrid functionals.²⁶

to **H**, and -15.1 kcal/mol for **E** to **I**, respectively) calculated from $2[(\text{L})_2\text{Fe}(\text{SH})_2]^- (\text{A/C/E}) \rightarrow 2\text{H}_2\text{S} + [(\text{L})_2\text{Fe}(\mu\text{-S})_2\text{Fe}(\text{L})_2]^{2-} (\text{G/H/I})$ ($\text{L} = \text{NO}, \text{SH}$) also reflect that complex **5** prefers to dimerize into complex **6** via a large exothermic pathway, compared to small energy differences between MNIC **3** and dinuclear MNIC **4** (and between DNIC **1** and RRS **2**). That is, the preference of thermodynamic dimerization for complexes **1**, **3**, and **5** is in the order $5 > 3 > 1$.

CONCLUSION AND COMMENTS

A series of Fe^{III} –hydrosulfide DNIC, MNIC, and $[\text{2Fe2S}]$ clusters (that is, complexes **1**, **3**, **4**, **5**, and **6**) were synthesized and characterized by IR, UV–vis, ^1H NMR, EPR, SQUID measurements, XAS, and single-crystal X-ray diffraction.

Consistent with the previous S K-edge study on $[(\text{PhS})_2\text{Fe}(\text{NO})_2]^-$, $[(\text{PhS})_3\text{Fe}(\text{NO})]^-$, and $[\text{Fe}(\text{SPh})_4]^-$ showing the 2.75 oxidation state of Fe for $[(\text{PhS})_3\text{Fe}(\text{NO})]^-$ and 2.59 for $[(\text{PhS})_2\text{Fe}(\text{NO})_2]^-$,^{21a} DFT computation and the experimental (and calculated) reduction potential ($E_{1/2}$) of DNIC 1, MNIC 3, and complex 5 unambiguously show that triplet NO^- acts as a stronger electron-donating ligand, compared to thiolate, to reduce the Z_{eff} of the iron center and stabilize DNIC 1 to prevent dimerization as well as reduction of Fe^{III} by $[\text{HS}]^-$ -coordinate ligands. This result indicates that the thermal stability of mononuclear complexes 1, 3, and 5 containing the $[\text{Fe}^{\text{III}}-\text{SH}]$ motif is in the order $1 > 3 > 5$. Moreover, the reaction free energies obtained from DFT computation (-0.6 kcal/mol for A to G, -6.8 kcal/mol for C to H, and -15.1 kcal/mol for E to I) also reflect that the preference of thermodynamic dimerization for complexes 1, 3, and 5 is in the order $5 > 3 > 1$.

The thermally unstable MNIC 3 and complex 5 in THF/DMF spontaneously dimerize into Fe^{III} -hydrosulfide complex 4 (^1H NMR chemical shift δ 3.49 ppm (SH, d_7 -DMF)) along with release of H_2S and complex 6 with ^1H NMR chemical shift δ 36.5 ppm (SH, d_7 -DMF) displaying an isotropic shift, respectively. That is, the electronic structure of complex 6 may be described as two Fe^{III} ($S = 5/2$) centers antiferromagnetically coupled to yield an $S = 0$ ground state with thermal occupancy of higher spin states (the corresponding $\chi_{\text{M}}T$ value decreases as a function of the temperature to $0.036 \text{ cm}^3 \text{ K mol}^{-1}$ at 95 K),^{30b} compared to that of complex 4 described as two $\{\text{Fe}(\text{NO})\}^7$ motifs antiferromagnetically coupled. These results and conclusion are supported by the Heisenberg J coupling constants ($H = JS_{\text{A}}S_{\text{B}}$) derived from the Yamaguchi equation.⁴⁰ That is, a greater number of NO ligands bound to the $[\text{2Fe}_2\text{S}]$ core leads to a larger antiferromagnetic coupling constant (4322 cm^{-1} for G, 813 cm^{-1} for H, and 415 cm^{-1} for I). In contrast to complex 6 spontaneously converting into the $[\text{Fe}_4\text{S}_4(\text{SH})_4]^{2-}$ cluster in DMF/MeCN at ambient temperature, the stabilization of complex 4 may also implicate that the noninnocent NO-coordinate ligand(s) bound to the $[(\text{HS})\text{Fe}(\mu\text{-S})_2\text{Fe}(\text{SH})]$ motif serves as an effective regulator to reduce the Z_{eff} of iron and to prevent the reductive elimination of the $\text{Fe}^{\text{III}}-\text{SH}$ bond.

Upon DNIC 1 being dissolved in water at ambient temperature, the rapid formation of RRS along with release of H_2S probed by NBD-SCN may signify DNIC 1 serves a role in the storage and transport of H_2S in the hydrophobic domain and may release H_2S in hydrophilic conditions in biological systems. Presumably, $[\text{HS}]^-$ in biology may most frequently bind to iron metal according to the preference dictated by the noninnocent characteristic of the coordinated NO ligands. The hydrosulfide-coordinated DNIC and MNIC may serve not only a role in H_2S storage/transport but also as the sulfide carrier/source in the synthesis of the $[\text{Fe}-\text{S}]$ cluster, although cysteine persulfide (Cys-SSH, a source of H_2S in the presence of a reducing agent) on cysteine desulfurase (IscS) is known to deliver its sulfane sulfur for the assembly of $[\text{Fe}-\text{S}]$ clusters on the scaffold protein (IscU).⁴²

EXPERIMENTAL SECTION

Manipulations, reactions, and transfers were conducted under nitrogen according to the Schlenk technique or in a glovebox (nitrogen gas). Solvents were distilled under nitrogen from appropriate drying agents (MeOH from I_2 and Mg, MeCN from CaH_2 , and hexane, diethyl ether, and tetrahydrofuran (THF) from sodium and benzophenone)

and stored in dried, N_2 -filled flasks over 4 Å molecular sieves. Nitrogen was purged through these solvents before use. Solvent was transferred to the reaction vessel via a stainless cannula under a positive pressure of N_2 . The reagents $\text{H}_2\text{S}(\text{g})$ (Chien-Fa), 18-crown-6-ether (TCI), bis(triphenylphosphoranylidene)ammonium chloride ([PPN][Cl]), 2-[4-(2-hydroxyethyl)piperazin-1-yl]ethanesulfonic acid (HEPES), D_2O (Sigma-Aldrich), and DMF (J. T. Baker) were used as received. Complexes $[\text{PPN}][(\text{tBuS})_3\text{Fe}(\text{NO})_2]$,¹⁷ $[\text{PPN}][(\text{EtS})_3\text{Fe}(\text{NO})]$,^{14c} $[\text{PPN}][(\text{tBuS})_3\text{Fe}(\text{NO})]$,^{14b} $[\text{PPN}][\text{Fe}(\text{SEt})_4]$,^{29b} [K-18-crown-6-ether] $[(\text{EtS})_2\text{Fe}(\text{NO})_2]$,^{14c} and NBD-SCN⁴³ were synthesized by published procedures. Infrared spectra of the ν_{NO} stretching frequencies were recorded on a PerkinElmer model Spectrum One B spectrometer with sealed solution cells (0.1 mm, CaF_2 windows) or KBr. UV-vis spectra were recorded on a Jasco V-570 spectrometer. ^1H NMR spectra were acquired on a Varian UNITY INOVA 500 NMR spectrometer. Analyses of carbon, hydrogen, and nitrogen were obtained with a CHN analyzer (Heraeus).

Preparation of [K-18-crown-6-ether] $[(\text{HS})_2\text{Fe}(\text{NO})_2]$ (1) and $[\text{PPN}][(\text{HS})_2\text{Fe}(\text{NO})_2]$ (1-PPN). The complex [K-18-crown-6-ether] $[(\text{EtS})_2\text{Fe}(\text{NO})_2]$ (0.2166 g, 0.4 mmol) (or $[\text{PPN}][(\text{tBuS})_2\text{Fe}(\text{NO})_2]$ (0.3207 g, 0.4 mmol)) was dissolved in THF (10 mL), and dry H_2S (excess) was then injected into the THF solution of $[(\text{EtS})_2\text{Fe}(\text{NO})_2]^-$ with a gastight syringe. The reaction solution was stirred under a N_2 atmosphere at ambient temperature for 5 min. The color of the reaction solution changed from brown to dark green. The IR ν_{NO} stretching frequencies shifting from 1715 s and 1674 s to 1735 s and 1686 cm^{-1} (THF) were assigned to the formation of 1 (or 1-PPN). The dark green solution was filtered through Celite, and hexane was then added to the filtrate to precipitate a dark green solid (yield 0.151 g (77%) for 1 and 0.235 g (85%) for 1-PPN). The cyclic voltammogram of the complex 1-PPN in 20 mM MeCN with 0.1 M $[n\text{-Bu}_4\text{N}][\text{PF}_6]$ as the supporting electrolyte at room temperature and at a scan rate of 500 mV/s shows a quasi-reversible redox wave with $E_{1/2} = -1.55 \text{ V}$ (vs $\text{Cp}_2\text{Fe}^+/\text{Cp}_2\text{Fe}$) and $i_{\text{pa}}/i_{\text{pc}} = 0.83$. Recrystallization from a THF solution of complex 1 layered with diethyl ether-hexane at -20°C for a week gives dark green crystals, suitable for XRD analysis. Attempts to measure the IR ν_{SH} stretching frequency in KBr were unsuccessful. IR ν_{NO} (cm^{-1}): 1735 s, 1686 s (THF); 1746 s, 1695 s (MeCN). Absorption spectrum (THF) [nm , λ_{max} ($\text{M}^{-1} \text{ cm}^{-1}$, ϵ): 333 (3000), 382 (2600), 732 (300). Anal. Calcd for $\text{C}_{36}\text{H}_{32}\text{FeN}_3\text{O}_2\text{P}_2\text{S}_2$ (1-PPN) C, 60.01; H, 4.48; N, 5.83. Found: C, 60.17; H, 4.66; N, 5.92.

Detection of the Released H_2S from an Aqueous Solution of 1 by Using the H_2S Probe NBD-SCN. To a flask of 1 (0.0485 g, 0.1 mmol) was added D_2O (5 mL) to dissolve complex 1. The color of the solution changed from green to dark red-brown. The IR stretching frequencies ν_{NO} shifting to 1713 s br and 1689 s br cm^{-1} (D_2O) were consistent with the formation of the known [K-18-crown-6-ether] $[(\text{NO})_2\text{Fe}(\mu\text{-S})_2]$ (2) (RRS).²⁸ To prove H_2S release derived from the aqueous solution of complex 1, the H_2S probe NBD-SCN was used since NBD-SCN reacts with complex 1 to produce NBD-SH in aprotic solvent THF at room temperature. Complex 1 (0.001 mmol) was prepared under a N_2 atmosphere in a vial. The vial containing complex 1 was then placed in a larger vial containing a mixture of a MeOH (0.2 mL) solution of NBD-SCN (0.001 mmol) and 9.8 mL of HEPES buffer (40 mM, pH 7.4) at room temperature. The larger vial was then capped with a well-sealed septum. HEPES buffer (2 mL, pH 7.4) was then added to the vial containing complex 1 with a syringe. After the solution was stirred for 4 h, NBD-SH was produced and detected by UV-vis spectroscopy. On the basis of the absorption intensity of NBD-SH at 530 nm obtained from NBD-SCN (100 μM) and $[\text{Na}][\text{SH}]$ (10, 20, 30, ..., 100 μM) (a standard curve), the amount of released H_2S derived from the aqueous solution of complex 1 at ambient temperature was quantified as 55% (Supporting Information Figure S6).

Preparation of $[\text{PPN}][(\text{HS})_3\text{Fe}(\text{NO})]$ (3) and Its Transformation into $[\text{PPN}]_2[(\text{NO})(\text{SH})\text{Fe}(\mu\text{-S})_2]$ (4). The complex $[\text{PPN}][(\text{EtS})_3\text{Fe}(\text{NO})]$ (0.3107 g, 0.4 mmol) (or $[\text{PPN}][(\text{tBuS})_3\text{Fe}(\text{NO})]$ (0.3444 g, 0.4 mmol)) was dissolved in THF (10 mL). Dry H_2S (excess) was then injected into the THF solution of the complex

[PPN][(EtS)₃Fe(NO)] with a gastight syringe at ambient temperature. The color of the reaction solution changed from dark red to dark yellow. The appearance of IR ν_{NO} = 1728 s cm⁻¹ (THF) indicated the formation of the thermally unstable **3**. After the dark yellow solution was stirred at ambient temperature overnight, the green solid **4** precipitated from the THF solution accompanied by release of H₂S probed by NBD-SCN. The precipitate was collected and redissolved in MeCN. The IR ν_{NO} stretching frequencies 1683 sh and 1668 s cm⁻¹ (MeCN) suggest the formation of complex **4**. Recrystallization from the MeCN solution of complex **4** layered with diethyl ether at -20 °C for a week yields dark green crystals (yield 0.15 g, 54%), suitable for XRD analysis. Attempts to measure the IR ν_{SH} stretching frequency of complex **4** in KBr were unsuccessful. IR ν_{NO} (cm⁻¹): 1683 sh, 1668 s (MeCN); 1671 s, 1651 vs (KBr). Absorption spectrum (MeCN) [nm, λ_{max} (M⁻¹ cm⁻¹, ϵ): 329 (8900), 407 (4500), 585 sh (1700). ¹H NMR (500 MHz, *d*₇-DMF, 25 °C, TMS): δ 3.49 ppm (s br, SH). Anal. Calcd for C₇₂H₆₃Fe₂N₄O₂P₄S₄: C, 62.70; H, 4.53; N, 4.06. Found: C, 63.02; H, 4.69; N, 3.48.

Preparation of [PPN]₂[(SH)₂Fe(μ -S)]₂ (6**).** The complex [PPN]-[Fe(SET)₄] (0.3232 g, 0.4 mmol) was loaded into a Schlenk flask (20 mL) and dissolved in DMF (10 mL) at room temperature. Dry H₂S (excess) was injected into the DMF solution of the complex [PPN][Fe(SET)₄] to yield a dark yellow-brown solution at 25 °C. The EPR spectrum displaying *g* values of 9.30 and 4.29 (DMF, 4 K) (*g* values of 9.6 and 4.30 (MeCN, 4 K)) is attributed to the formation of [PPN][Fe(SH)₄] (**5**). The rapid transformation of the DMF solution of complex **5** occurred over the course of 5 min to give **6** monitored by UV-vis at ambient temperature. X-ray-quality crystals were obtained by layering the MeCN solution of complex **6** with diethyl ether at -20 °C for 3 days. Conversion of complex **6** into the known [Fe₂S₄(SH)₄]²⁻ identified by UV-vis and ¹H NMR spectroscopy (δ 47.0 ppm (s br, SH) *d*₇-DMF, 25 °C, TMS) was observed when complex **6** was dissolved in DMF or MeCN at room temperature overnight (Supporting Information Figure S13b). Attempts to measure the IR ν_{SH} stretching frequency of complex **6** in KBr were unsuccessful. ¹H NMR (500 MHz, *d*₇-DMF, 25 °C, TMS): δ 36.5 ppm (s br, SH). Absorption spectrum (MeCN) [nm, λ_{max} (M⁻¹ cm⁻¹, ϵ): 309 (6345), 397 (4185), 433 (3351), 482 sh (1932), 585 sh (1360), 656 sh (677). Anal. Calcd for C₇₂H₆₄Fe₂N₂P₄S₆: C, 62.43; H, 4.66; N, 2.02. Found: C, 62.18; H, 4.42; N, 2.36.

EPR Measurements. EPR measurements were performed at the X-band using a Bruker E580 spectrometer equipped with a Bruker ELEXSYS super-high-sensitivity cavity. X-band EPR spectra of a THF solution of complex **1** (1-PPN) in a 4 mm EPR tube at 298 K were obtained with a microwave power of 15.000 (19.971) mW, frequency of 9.658817 (9.496315) GHz, conversion time of 20.39 (20.48) ms, receiver gain of 10, and modulation amplitude of 0.8 G at 100 kHz. X-band EPR spectra of a THF solution of complex **1** (1-PPN) in a 4 mm EPR tube at 77 K were obtained with a microwave power of 15.000 (19.971) mW, frequency of 9.656525 (9.494421) GHz, conversion time of 20.39 (81.92) ms, receiver gain of 10, and modulation amplitude of 0.8 G at 100 kHz. X-band EPR spectra of complex **3** in THF placed in a 4 mm EPR tube at 4 K were obtained with a microwave power of 15.000 mW, frequency of 9.460709 GHz, conversion time of 20.39 ms, receiver gain of 30, and modulation amplitude of 1.6 G at 100 kHz. X-band EPR spectra of complex **5** in DMF placed in a 4 mm EPR tube at 4 K were obtained with a microwave power of 15.000 mW, frequency of 9.462448 GHz, conversion time of 81.79 ms, receiver gain of 30, and modulation amplitude of 1.6 G at 100 kHz.

X-ray Absorption Measurements. All X-ray absorption experiments were carried out at the National Synchrotron Radiation Research Center (NSRRC), Hsinchu, Taiwan. Fe K-edge spectra were recorded at room temperature. The data were averaged, and a smooth background was removed from all spectra by fitting a straight line to the pre-edge region and subtracting this straight line from the entire spectrum. Normalization of the data was accomplished by fitting a flat polynomial to the postregion and normalizing the edge jump to 1.0 at 7400 eV. For Fe K-edge measurements, experiments were performed in transmission mode at the BL17C wiggler beamline with a double-

crystal Si(111) monochromator. The energy resolution $\Delta E/E$ was estimated to be about 2×10^{-4} . High harmonics were rejected by Rh-coated mirrors. The spectra were scanned from 6.912 to 7.972 keV. A reference Fe foil is always measured simultaneously, in which the first inflection point at 7112.0 eV of the Fe foil spectrum is used for energy calibration. Ion chambers used to measure the incident (*I*₀) and transmitted (*I*) beam intensities were filled with a mixture of N₂ and He gases and a mixture of N₂ and Ar gases, respectively.

Crystallography. The crystals of complexes **1**, **1-PPN**, **4**, and **6** chosen for X-ray diffraction study were measured in sizes of $0.15 \times 0.13 \times 0.07$, $0.36 \times 0.32 \times 0.21$, $0.30 \times 0.30 \times 0.25$, and $0.12 \times 0.10 \times 0.07$ mm, respectively. The crystals were mounted on a glass fiber. Unit-cell parameters were obtained by least-squares refinement. Diffraction measurements for complexes **1**, **1-PPN**, **4**, and **6** were carried out on a Bruker Kappa Apex II diffractometer with graphite-monochromated Mo *K* α radiation (λ = 0.7107 Å) and between 1.98° and 25.05° for **1** (between 2.37° and 25.03° for **1-PPN**, between 1.148° and 26.433° for **4**, and between 1.149° and 26.537° for **6**). Least-squares refinement of the positional and anisotropic thermal parameters of all non-hydrogen atoms and fixed hydrogen atoms was based on *F*². The SHELXTL structure refinement program was employed.⁴⁴ A summary of the crystallographic data, intensity collection, and structure refinement parameters for complexes **1**, **1-PPN**, **4**, and **6** are collected in Supporting Information Table S4.

Magnetic Measurements. The magnetic data of the powdered samples of complex **6** were recorded on a SQUID magnetometer (SQUID-VSM, Quantum Design) under an external magnetic field (0.1 T) in the temperature range of 2–300 K. The magnetic susceptibility data were corrected with the ligands' diamagnetism by the tabulated Pascal constants.

Computational Details. All DFT calculations were performed with the Gaussian 09 program.⁴⁵ All geometry optimizations of conformations A–F were conducted with DFT using the BP86 functional³³ and a mixed basis set of SDD ECP³⁴ on Fe, BSX-LANL³⁵ on S, and 6-311++G(d,p)³⁶ on all other atoms. The methodology was chosen because it has been shown to have good accuracy for the DNIC system.³⁷ For solvent correction a PCM model with acetonitrile (ϵ = 35.688) was applied.⁴⁶ According to the EPR data of complexes **1**, **3**, and **5**, the spin states of conformations A, C, and E were assigned as *S* = 1/2, 3/2, and 5/2, respectively. Since conformations B and E are similar to [(EtS)₂Fe(NO)₂]²⁻ and [Fe(SET)₄]²⁻,^{20b,39} the spin states of their reduced forms were assigned as *S* = 0 and 2, respectively. Despite the lack of a structure for [(EtS)₃Fe(NO)]²⁻, the spin state of conformation D was expected to be *S* = 1 derived from a high-spin Fe^{II} (*S*_{Fe} = 2) antiferromagnetically coupled with a nitroxyl ligand (NO⁻) (*S*_{NO} = 1). For singlet conformations G–I, the BS DFT method was employed.^{26,38a} First, high-spin (HS) states (*S* = 1 for G, *S* = 3 for H, and *S* = 5 for I) were optimized. Subsequently, a flip of the spin on selected atoms for an initial guess of the antiferromagnetically coupled state was conducted, followed by geometry optimization to generate the broken-symmetry *M*_s = 0 state.²⁶ The “stable” keyword was used to test the stability of the wave function. Frequency calculations were carried out for detected stationary points to ensure that they correspond to the true minima on the potential energy hypersurface. The thermal correction to the Gibbs free energy was made under the conditions of 298.15 K and 1 atm. The Heisenberg *J* coupling constant (*H* = *J**S*_A*S*_B) was estimated by using the Yamaguchi approach: *J* = 2(*E*_{HS} - *E*_{BS})/((*S*²)_{HS} - (*S*²)_{BS}),⁴⁰ in which *E*_{HS} - *E*_{BS} is energy difference between the high-spin and low-spin states, and (*S*²)_{HS} and (*S*²)_{BS} are the expectation values of the HS and BS *S*² operators. Due to the very strong antiferromagnetic coupling in conformation G, the BP86 wave function collapses into a spin-restricted solution, similarly to the OLYP wave function in the previous study.²⁶ The spin density map was plotted with the Chemissian 3.3 program.⁴⁷ The natural charge analysis was obtained from the NBO 5.9 program in the Gaussian 09 package.⁴⁸

■ ASSOCIATED CONTENT

■ Supporting Information

IR, UV-vis, ^1H NMR, EPR, and XAS spectra, cyclic voltammograms, crystallographic and computational details, and CIF data. This material is available free of charge via the Internet at <http://pubs.acs.org>.

■ AUTHOR INFORMATION

Corresponding Authors

cctsou0327@gmail.com

wfliaw@mx.nthu.edu.tw

Notes

The authors declare no competing financial interest.

■ ACKNOWLEDGMENTS

We gratefully acknowledge financial support from the Ministry of Science and Technology (Taiwan). We thank Dr. Jyh-Fu Lee, the National Synchrotron Radiation Research Center of Taiwan (NSRRC), and the National Center for High-Performance Computing (NCHC) for their support of the hardware and software applied in this work. We also thank Mr. Ting-Shen Kuo and Mrs. Pei-Lin Chen for the single-crystal X-ray structural determinations.

■ REFERENCES

- (1) (a) Szabo, C. *Nat. Rev. Drug Discovery* **2007**, *6*, 917–935. (b) Li, L.; Moore, P. K. *Trends Pharmacol. Sci.* **2008**, *29*, 84–90. (c) Li, X.; Bazer, F. W.; Gao, H.; Jobgen, W.; Johnson, G. A.; Li, P.; McKnight, J. R.; Satterfield, M. C.; Spencer, T. E.; Wu, G. *Amino Acids* **2009**, *37*, 65–78. (d) Martelli, A.; Testai, L.; Breschi, M. C.; Blandizzi, C.; Viridis, A.; Taddei, S.; Calderone, V. *Med. Res. Rev.* **2012**, *32*, 1093–1130. (e) Kolluru, G. K.; Shen, X.; Bir, S. C.; Kevil, C. G. *Nitric Oxide* **2013**, *35*, 5–20. (f) Shatalin, K.; Shatalina, E.; Mironov, A.; Nudler, E. *Science* **2011**, *334*, 986–990.
- (2) (a) Li, Q.; Lancaster, J. R., Jr. *Nitric Oxide* **2013**, *35*, 21–34. (b) Bruce King, S. *Free Radical Biol. Med.* **2013**, *55*, 1–7.
- (3) Coletta, C.; Papapetropoulos, A.; Erdelyi, K.; Olah, G.; Modis, K.; Panopoulos, P.; Asimakopoulou, A.; Gero, D.; Sharina, I.; Martin, E.; Szabo, C. *Proc. Natl. Acad. Sci. U.S.A.* **2012**, *109*, 9161–9166.
- (4) Filipovic, M. R.; Miljkovic, J.; Nauser, T.; Royzen, M.; Klos, K.; Shubina, T.; Koppenol, W. H.; Lippard, S. J.; Ivanovic-Burmazovic, I. *J. Am. Chem. Soc.* **2012**, *134*, 12016–12027.
- (5) (a) Filipovic, M. R.; Ivanovic-Burmazovic, I. *Chem.—Eur. J.* **2012**, *18*, 13538–13540. (b) Miljkovic, J. L.; Kenkel, I.; Ivanovic-Burmazovic, I.; Filipovic, M. R. *Angew. Chem., Int. Ed.* **2013**, *52*, 12061–12064.
- (6) (a) Ma, E. S.; Rettig, S. J.; Patrick, B. O.; James, B. R. *Inorg. Chem.* **2012**, *51*, 5427–5434. (b) Perez-Torrente, J. J.; Jimenez, M. V.; Hernandez-Gruel, M. A.; Fabra, M. J.; Lahoz, F. J.; Oro, L. A. *Chem.—Eur. J.* **2009**, *15*, 12212–12222. (c) Mudalige, D. C.; Ma, E. S.; Rettig, S. J.; James, B. R.; Cullen, W. R. *Inorg. Chem.* **1997**, *36*, 5426–5427. (d) Sellman, D.; Lechner, P.; Knoch, F.; Moll, M. *Angew. Chem., Int. Ed. Engl.* **1991**, *30*, 552–553.
- (7) Galardon, E.; Roger, T.; Deschamps, P.; Roussel, P.; Tomas, A.; Artaud, I. *Inorg. Chem.* **2012**, *51*, 10068–10070.
- (8) (a) Venkateswara, P.; Holm, R. H. *Chem. Rev.* **2004**, *104*, 527–559. (b) Kuwata, S.; Hidai, M. *Coord. Chem. Rev.* **2001**, *213*, 211–305.
- (9) (a) Jove, F. A.; Pariya, C.; Scoblete, M.; Yap, G. P.; Theopold, K. H. *Chem.—Eur. J.* **2011**, *17*, 1310–1318. (b) Pavlik, J. W.; Noll, B. C.; Oliver, A. G.; Schulz, C. E.; Scheidt, W. R. *Inorg. Chem.* **2010**, *49*, 1017–1026. (c) Dhifet, M.; Belkhiria, M. S.; Daran, J. C.; Nasri, H. *Acta Crystallogr., Sect. E* **2009**, *65*, m967–m968. (d) Arif, A. M.; Hefner, J. G.; Jones, R. A.; Koschmieder, S. U. *J. Coord. Chem.* **1991**, *23*, 13–19. (e) Vaira, M. D.; Midollini, S.; Sacconi, L. *Inorg. Chem.* **1977**, *16*, 1518–1524. (f) Cai, L.; Holm, R. H. *J. Am. Chem. Soc.* **1994**, *116*, 7177–7188.
- (10) English, D. R.; Hendrickson, D. N.; Suslick, K. S.; Eigenbrot, C. W.; Scheidt, W. R. *J. Am. Chem. Soc.* **1984**, *106*, 7258–7259.
- (11) Balch, A. L.; Cornman, C. R.; Safari, N. *Organometallics* **1990**, *9*, 2420–2421.
- (12) (a) Szaciłowski, K.; Chmura, A.; Stasicka, Z. *Coord. Chem. Rev.* **2005**, *249*, 2408–2436. (b) Butler, A. R.; Megson, I. L. *Chem. Rev.* **2002**, *102*, 1155–1165. (c) Vanin, A. F. *Nitric Oxide* **2009**, *21*, 1–13. (d) Tonzetich, Z. J.; McQuade, L. E.; Lippard, S. J. *Inorg. Chem.* **2010**, *49*, 6338–6348.
- (13) (a) Kennedy, M. C.; Antholine, W. E.; Beinert, H. *J. Biol. Chem.* **1997**, *272*, 20340–20347. (b) Foster, M. W.; Cowan, J. A. *J. Am. Chem. Soc.* **1999**, *121*, 4093–4100. (c) Rogers, P. A.; Eide, L.; Klungland, A.; Ding, H. *DNA Repair* **2003**, *2*, 809–817. (d) Sellers, V. M.; Johnson, M. K.; Dailey, H. A. *Biochemistry* **1996**, *35*, 2699–2704. (e) Ding, H.; Dimple, B. *Proc. Natl. Acad. Sci. U.S.A.* **2000**, *97*, 5146–5150.
- (14) (a) Koch, S. A.; Maelia, L. E. *J. Am. Chem. Soc.* **1983**, *105*, 5944–5945. (b) Harrop, T. C.; Song, D.; Lippard, S. J. *J. Am. Chem. Soc.* **2006**, *126*, 3528–3529. (c) Lu, T.-T.; Chiou, S.-J.; Chen, C.-Y.; Liaw, W.-F. *Inorg. Chem.* **2006**, *45*, 8799–8806.
- (15) Harrop, T. C.; Song, D.; Lippard, S. J. *J. Inorg. Biochem.* **2007**, *101*, 1730–1738.
- (16) (a) Chu, C. T.-W.; Dahl, L. F. *Inorg. Chem.* **1977**, *16*, 3245–3251. (b) Weatherill, T. D.; Rauchfuss, T. B.; Scott, R. A. *Inorg. Chem.* **1986**, *25*, 1466–1472.
- (17) Tsou, C.-C.; Lu, T.-T.; Liaw, W.-F. *J. Am. Chem. Soc.* **2007**, *129*, 12626–12627.
- (18) (a) Tsou, C. C.; Tsai, F. T.; Chen, H. Y.; Hsu, I. J.; Liaw, W. F. *Inorg. Chem.* **2013**, *52*, 1631–1639. (b) Hung, M.-C.; Tsai, M.-C.; Liaw, W.-F. *Inorg. Chem.* **2006**, *45*, 6041–6047.
- (19) Lu, T.-T.; Tsou, C.-C.; Huang, H.-W.; Hsu, I.-J.; Chen, J.-M.; Kuo, T.-S.; Wang, Y.; Liaw, W.-F. *Inorg. Chem.* **2008**, *47*, 6040–6050.
- (20) (a) Tsai, M.-C.; Tsai, F.-T.; Lu, T.-T.; Tsai, M.-L.; Wei, Y.-C.; Hsu, I.-J.; Lee, J.-F.; Liaw, W.-F. *Inorg. Chem.* **2009**, *48*, 9579–9591. (b) Yeh, S.-W.; Lin, C.-W.; Li, Y.-W.; Hsu, I.-J.; Chen, C.-H.; Jang, L.-Y.; Lee, J.-F.; Liaw, W.-F. *Inorg. Chem.* **2012**, *51*, 4076–4087.
- (21) (a) Lu, T.-T.; Lai, S.-H.; Li, Y.-W.; Hsu, I.-J.; Jang, L.-Y.; Lee, J.-F.; Chen, I.-C.; Liaw, W.-F. *Inorg. Chem.* **2011**, *50*, 5396–5406. (b) Hopmann, K. H.; Conradie, J.; Ghosh, A. *J. Phys. Chem. B* **2009**, *113*, 10540–10547. (c) Ye, S.; Neese, F. *J. Am. Chem. Soc.* **2010**, *132*, 3646–3647.
- (22) (a) Thomas, J. T.; Robertson, J. H.; Cox, E. G. *Acta Crystallogr.* **1958**, *11*, 599–604. (b) Sanina, N. A.; F, O. S.; Aldoshin, S. M.; Ovanesyana, N. S. *Russ. Chem. Bull.* **2000**, 1109–1112.
- (23) Montoya, L. A.; Pearce, T. F.; Hansen, R. J.; Zakharov, L. N.; Pluth, M. D. *J. Org. Chem.* **2013**, *78*, 6550–6557.
- (24) (a) Li, M.; Bonnet, D.; Bill, E.; Neese, F.; Weyhermüller, T.; Blum, N.; Sellmann, D.; Wieghardt, K. *Inorg. Chem.* **2002**, *41*, 3444–3456. (b) Conradie, J.; Quarless, D. A. J.; Hsu, H.-F.; Harrop, T. C.; Lippard, S. J.; Koch, S. A.; Ghosh, A. *J. Am. Chem. Soc.* **2007**, *129*, 10446–10456.
- (25) (a) Tsou, C. C.; Yang, W. L.; Liaw, W. F. *J. Am. Chem. Soc.* **2013**, *135*, 18758–18761. (b) Tsai, F.-T.; Chen, P.-L.; Liaw, W.-F. *J. Am. Chem. Soc.* **2010**, *132*, 5290–5299.
- (26) Hopmann, K. H.; Noodleman, L.; Ghosh, A. *Chem.—Eur. J.* **2010**, *16*, 10397–10408.
- (27) (a) Harrop, T. C.; Tonzetich, Z. J.; Reisner, E.; Lippard, S. J. *J. Am. Chem. Soc.* **2008**, *130*, 15602–15610. (b) Tennyson, A. G.; Dhar, S.; Lippard, S. J. *J. Am. Chem. Soc.* **2008**, *130*, 15087–15098.
- (28) Lu, T.-T.; Huang, H.-W.; Liaw, W.-F. *Inorg. Chem.* **2009**, *48*, 9027–9035.
- (29) (a) Maelia, L. E.; Millar, M.; Koch, S. A. *Inorg. Chem.* **1992**, *31*, 4594–4600. (b) Chang, S.; Koch, S. A. *J. Inorg. Biochem.* **2007**, *101*, 1758–1759.
- (30) (a) Noodleman, L.; Case, D. A.; Aizman, A. *J. Am. Chem. Soc.* **1988**, *110*, 1001–1005. (b) Gillum, W. O.; Frankel, R. B.; Foner, S.; Holm, R. H. *Inorg. Chem.* **1976**, *15*, 1095–1100.
- (31) Hoveyda, H. R.; Holm, R. H. *Inorg. Chem.* **1997**, *36*, 4571–4578.

- (32) (a) Claser, T. G.; Rose, K.; Shadle, S. E.; Hedman, B.; Hodgson, K. O.; Solomon, E. I. *J. Am. Chem. Soc.* **2001**, *123*, 442–454. (b) Rose, K.; Shadle, S. E.; Glaser, T.; de Vries, S.; Cherepanov, A.; Canters, G. W.; Hedman, B.; Hodgson, K. O.; Solomon, E. I. *J. Am. Chem. Soc.* **1999**, *121*, 2353–2363.
- (33) (a) Perdew, J. P.; Yang, W. *Phys. Rev. B* **1986**, *33*, 8800–8802. (b) Becke, A. D. *Phys. Rev. A* **1988**, *38*, 3098–3100.
- (34) Perdew, J. P. *Phys. Chem. Chem. Phys.* **1986**, *33*, 8822–8824.
- (35) Check, C. E.; Faust, T. O.; Bailey, J. M.; Wright, B. J.; Gilbert, T. M.; Sunderlin, L. S. *J. Phys. Chem. A* **2001**, *105*, 8111–8116.
- (36) (a) Hay, P. J. *J. Chem. Phys.* **1977**, *66*, 4377–4384. (b) Krishnan, R.; Binkley, J. S.; Seeger, R.; Pople, J. A. *J. Chem. Phys.* **1980**, *72*, 650–654. (c) Raghavachari, K.; Trucks, G. W. *J. Chem. Phys.* **1989**, *91*, 1062–1065. (d) Wachters, A. J. H. *J. Chem. Phys.* **1970**, *52*, 1033–1037.
- (37) Brothers, S. M.; Darensbourg, M. Y.; Hall, M. B. *Inorg. Chem.* **2011**, *50*, 8532–8540.
- (38) (a) Schmitt, E. A.; Noodleman, L.; Baerends, E. J.; Hendrickson, D. N. *J. Am. Chem. Soc.* **1992**, *114*, 6109–6119. (b) Hopmann, K. H.; Ghosh, A.; Noodleman, L. *Inorg. Chem.* **2009**, *48*, 9155–9165. (c) Jaworska, M.; Stasicka, Z. *New J. Chem.* **2005**, *29*, 604–612.
- (39) Hagen, K. S.; Watson, A. D.; Holm, R. H. *J. Am. Chem. Soc.* **1983**, *105*, 3905–3913.
- (40) Soda, T.; Kitagawa, Y.; Onishi, T.; Takano, Y.; Shigeta, Y.; Nagao, H.; Yoshioka, Y.; Yamaguchi, K. *Chem. Phys. Lett.* **2000**, *319*, 223–230.
- (41) (a) Suzuki, N.; Higuchi, T.; Urano, Y.; Kikuchi, K.; Uekusa, H.; Ohashi, Y.; Uchida, T.; Kitagawa, T.; Nagano, T. *J. Am. Chem. Soc.* **1999**, *121*, 11571–11572. (b) Das, P. K.; Chatterjee, S.; Samanta, S.; Dey, A. *Inorg. Chem.* **2012**, *51*, 10704–10714.
- (42) (a) Johnson, D. C.; Dean, D. R.; Smith, A. D.; Johnson, M. K. *Annu. Rev. Biochem.* **2005**, *74*, 247–281. (b) Lill, R.; Muhlenhoff, U. *Trends Biochem. Sci.* **2005**, *30*, 133–141. (c) Rouault, T. A.; Tong, W.-H. *Nat. Rev. Mol. Cell Biol.* **2005**, *6*, 345–351.
- (43) Chen, Y. H.; Tsai, J. C.; Cheng, T. H.; Yuan, S. S.; Wang, Y. M. *Biosens. Bioelectron.* **2014**, *56*, 117–123.
- (44) Sheldrick, G. M. *SHELXTL, Program for Crystal Structure Determination*; Siemens Analytical X-ray Instruments Inc.: Madison, WI, 1994.
- (45) Frisch, M. J.; Trucks, G. W.; Schlegel, H. B.; Scuseria, G. E.; Robb, M. A.; Cheeseman, J. R.; Montgomery, J. A., Jr.; Vreven, T.; Kudin, K. N.; Burant, J. C.; Millam, J. M.; Iyengar, S. S.; Tomasi, J.; Barone, V.; Mennucci, B.; Cossi, M.; Scalmani, G.; Rega, N.; Petersson, G. A.; Nakatsuji, H.; Hada, M.; Ehara, M.; Toyota, K.; Fukuda, R.; Hasegawa, J.; Ishida, M.; Nakajima, T.; Honda, Y.; Kitao, O.; Nakai, H.; Klene, M.; Li, X.; Knox, J. E.; Hratchian, H. P.; Cross, J. B.; Bakken, V.; Adamo, C.; Jaramillo, J.; Gomperts, R.; Stratmann, R. E.; Yazyev, O.; Austin, A. J.; Cammi, R.; Pomelli, C.; Ochterski, J. W.; Ayala, P. Y.; Morokuma, K.; Voth, G. A.; Salvador, P.; Dannenberg, J. J.; Zakrzewski, V. G.; Dapprich, S.; Daniels, A. D.; Strain, M. C.; Farkas, O.; Malick, D. K.; Rabuck, A. D.; Raghavachari, K.; Foresman, J. B.; Ortiz, J. V.; Cui, Q.; Baboul, A. G.; Clifford, S.; Cioslowski, J.; Stefanov, B. B.; Liu, G.; Liashenko, A.; Piskorz, P.; Komaromi, I.; Martin, R. L.; Fox, D. J.; Keith, T.; Al-Laham, M. A.; Peng, C. Y.; Nanayakkara, A.; Challacombe, M.; Gill, P. M. G.; Johnson, B.; Chen, W.; Wong, M. W.; Gonzalez, C.; Pople, J. A. *Gaussian 09*, revision A.02; Gaussian, Inc.; Wallingford, CT, 2009.
- (46) Miertus, S.; Scrocco, E.; Tomasi, J. *Chem. Phys.* **1981**, *55*, 117–129.
- (47) Chemissian v3.3, <http://www.chemissian.com> (accessed September 8, 2012).
- (48) (a) Foster, J. P.; Weinhold, F. *J. Am. Chem. Soc.* **1980**, *102*, 7211–7218. (b) Reed, A. E.; Weinstock, R. B.; Weinhold, F. *J. Chem. Phys.* **1985**, *83*, 735–746. (c) Reed, A. E.; Weinhold, F. *J. Chem. Phys.* **1983**, *78*, 4066–4073.